

CONTEX-T: Contextual Privacy Exploitation via Transformer Spectral Analysis for IoT Device Fingerprinting

Nazmul Islam and Mohammad Zulkernine

Abstract—The rapid expansion of internet of things (IoT) devices have created a pervasive ecosystem where encrypted wireless communications serve as the primary privacy and security protection mechanism. While encryption effectively protects message content, packet metadata and statistics inadvertently expose device identities and user contexts. Various studies have exploited raw packet statistics and their visual representations for device fingerprinting and identification. However, these approaches remain confined to the spatial domain with limited feature representation. Therefore, this paper presents CONTEX-T, a novel framework that exploits contextual privacy vulnerabilities using spectral representation of encrypted wireless traffic for IoT device characterization. The experiments show that spectral analysis provides new and rich feature representation for covert reconnaissance attacks, revealing a complex and expanding threat landscape that would require robust countermeasures for IoT security management. CONTEX-T first transforms raw packet length sequences into time-frequency spectral representations and then utilizes transformer-based spectral analysis for the device identification. We systematically evaluated multiple spectral representation techniques and transformer-based models across encrypted traffic samples from various IoT devices. CONTEX-T effectively exploited privacy vulnerabilities and achieved device classification accuracy exceeding 99% across all devices while remaining completely passive and undetectable.

Index Terms—Contextual Privacy, fingerprinting, IoT security, spectral analysis, vision transformer, wireless communication.

I. INTRODUCTION

THE exponential growth of Internet of Things (IoT) devices spans critical domains including smart homes, healthcare monitoring, industrial automation, and urban infrastructure. This growth establishes a ubiquitous digital ecosystem where wireless communications serve as the foundation for device interaction and data exchange [1]. To protect sensitive user information and operational data during the communication, encryption protocols such as Transport Layer Security (TLS), Secure Sockets Layer (SSL), and WiFi Protected Access (WPA) have become standard, forming the primary line of defense against payload-based eavesdropping and content analysis attacks [2]. While these cryptographic protections secure message content, they inadvertently expose a critical vulnerability. Encrypted traffic metadata remains visible to passive observers, enabling covert contextual privacy exploitation independent of encryption strength.

Contextual privacy exploitation is crucial for reconnaissance attack that serves as a covert initial step in the broader cyber kill chain [3]. These attacks operate through side-

channel analysis of traffic metadata, revealing device types, behavioral patterns, and even enumerate system vulnerabilities. Techniques such as passive packet sniffing can capture all packets traversing a wireless channel using commodity packet-capturing tools such as Wireshark, tcpdump, and Aircrack-ng [4]. Adversaries can intercept these encrypted network packets, extracting critical metadata including packet lengths, source MAC addresses, access points, traffic rates, and temporal patterns without triggering intrusion detection systems or requiring active network participation. Once adversaries compile these fingerprints, they can identify devices and exploitable vulnerabilities for subsequent attack in cyber kill chain. Unlike active scanning techniques (port scanning, service enumeration) that generate anomalous traffic volumes, passive sniffing blends seamlessly into legitimate network activity, providing attackers with persistent, undetected access to intelligence-gathering capabilities.

The vulnerability of encrypted traffic to metadata analysis for device fingerprinting and other forms of contextual exploitation is well established in prior research [5]. Building on this foundation, recent studies have introduced network traffic image analysis as a more effective alternative for device fingerprinting and identification. Visual analysis enhances feature extraction and representation while alleviating the limitations of manual feature engineering and scalability [6], [7], [8], [9]. These methods predominantly convert raw packet streams into spatially organized grayscale images, on which deep learning (DL) models are trained and tested. Such image-based approaches preserve byte-level sequential and spatial locality but fundamentally remain in the amplitude domain. While some temporal modeling techniques have been integrated into these frameworks, they fundamentally treat temporal dynamics (such as periodicity, harmonic structure, and frequency modulations) implicitly. Neural networks must learn to recognize periodicity, polling cycles, heartbeat intervals, and inter-packet timing patterns through data-driven feature extraction. This implicit learning paradigm lacks interpretability, requires large, annotated datasets to capture temporal periodicities, and provides no formal guarantees about which traffic characteristics enable device identification.

Despite the effectiveness of spatial-domain grayscale methods, the time-frequency domain provides enhanced feature representation and interpretability, as established in prior work across domains such as human activity recognition [10], emotion recognition [11], intrusion detection [12], [13], internet traffic analysis [14], and healthcare [15]. However, systematic application and evaluation of frequency-domain spectral

analysis for IoT device fingerprinting have not been addressed in existing literature to the best of our knowledge. Furthermore, the integration of Vision Transformers (ViTs) with spectrogram analysis introduces a new architectural paradigm for IoT fingerprinting. Unlike CNNs that capture local spatial correlations through convolutional kernels, ViTs leverage global self-attention mechanisms to model long-range dependencies across time-frequency representations. This enables the capture of distant spectral relationships (such as harmonics separated by multiple frequency bins and periodic bursts separated by time lags) [16].

Therefore, this paper presents CONTEX-T, a novel framework that exploits contextual privacy vulnerabilities in encrypted wireless IoT traffic through frequency-domain spectral analysis with rich feature representation. CONTEX-T systematically transforms raw packet-length sequences into time-frequency spectrograms via Short-Time Fourier Transform (STFT) and Continuous Wavelet Transform (CWT), extracting explicit information-theoretic features including spectral peaks, harmonic decomposition, instantaneous frequency, phase coherence, and wavelet variance. We evaluate state-of-the-art ViT architectures on these spectral representations, achieving superior device classification accuracy across encrypted traffic samples while maintaining complete passivity and undetectability. Through rigorous statistical validation using 95% bootstrap confidence intervals, we demonstrate that device-specific communication behaviors persist as spectral signatures even under strong encryption. Importantly, the proposed approach reveals a new threat landscape of spectral analysis with rich feature representation that adversaries may exploit for passive reconnaissance and device fingerprinting. The primary contributions of this paper are:

- Frequency-Domain Feature Extraction: Introduction of spectrogram-based representation of encrypted packet-length sequences via STFT and CWT, exposing device-specific periodicities, harmonic patterns, and temporal dynamics as explicit spectral features rather than implicitly learned representations.
- Transformer Architecture Benchmarking: Systematic evaluation of ViT models with rigorous statistical validation via 95% bootstrap confidence intervals. This determines the optimal combinations of spectral resolution, segment length, and overlap for best performance.
- Generalization and Cross-Configuration Evaluation: Comprehensive robustness analysis assessing model performance across held-out out-of-distribution (OOD) evaluation set. Identifying model configurations that maintain high accuracy with these datasets that reflect variable observation windows and establish practical limitations for adversarial reconnaissance scenarios.

The remainder of this paper is organized as follows: Section II surveys related work on traffic analysis attacks and IoT device fingerprinting. Section III provides the methodology for spectrogram generation and ViT models. Section IV formalizes the adversarial threat model and CONTEX-T framework. Section V reports experimental setup, evaluation, and cross-

configuration generalization. Section VI concludes the paper.

II. RELATED WORKS

The related studies are divided into two subsections, covering DL-based IoT fingerprinting from raw data and from image representations.

A. DL-Based IoT Fingerprinting from Raw Traffic

The earliest approaches to IoT device identification relied on direct analysis of packet-level features extracted from raw traffic. These methods leverage statistical properties, temporal patterns, and distributional characteristics of packet metadata to construct device fingerprints. Protocol-aware statistical features were used in [17] that rely on multiple flow attributes (volume, duration, and sleep time) together with protocol-specific signaling patterns (DNS queries, NTP timestamps, and cipher suites). The features are then processed with random forest models to classify IoT devices. However, the approach requires extensive protocol parsing and domain-specific expertise. The frequency distribution modeling of ByteIoT [18] eliminates protocol dependencies by distilling identification to packet-length frequency distributions processed via Hellinger distance-based k-nearest neighbor classification with DBSCAN clustering. This improved both computational efficiency and scalability through simple queries against compact distribution models. IoTDevID [19] advances cross-dataset generalization through systematic elimination of session-specific features, employing information-theoretic voting across six feature-importance techniques to identify 33 generalizable packet-level characteristics. It applied decision trees with MAC-based aggregation to solve the transfer problem for devices sharing gateway addresses. Time-series dictionary approach (ROCKET + HYDRA) in [20] streamlines feature extraction by applying 10,000 random convolutional kernels over multivariate packet-length sequences to capture multi-scale temporal patterns. It employed shuffle-split organization schemes to address severe data imbalance and enabling logistic regression classification with minimal computational overhead. MetaRockETC [21] extends this paradigm through meta-learning, leveraging model-agnostic meta-learning (MAML) over multivariate time-series representations (original, uplink/downlink, cumulative sums). This was processed through random convolution transformations with multiple pooling operators, demonstrating cross-task adaptability and rapid few-shot learning capabilities.

Despite these advances, all five methods rely on explicit feature extraction or transformation pipelines that either require domain expertise (statistical feature selection), extensive hyperparameter tuning (kernel transformations, distance metrics), or multi-stage processing (packet-level classification followed by aggregation), limiting end-to-end optimization and potentially leaving discriminative patterns unexploited [5]. This limitation motivates a paradigm shift toward spatial-domain representations, where raw packet sequences are reshaped into 2D grayscale images for DL analysis discussed in the following section.

B. DL-Based IoT Fingerprinting from Image Representations

Techniques in [6], [7], [8], [9] convert N-byte sessions into fixed-size grayscale images (typically 28×28 to 60×40), where each byte b_i directly maps to pixel intensity $I(x, y) = b_i$.

TABLE I
SUMMARY AND COMPARISON OF EXISTING LITERATURE

Reference	Feature Domain	Traffic Pattern Representation	Traffic Pattern Recognition	Information preserved	Interpretability	Metadata utilized	Robustness to Jitter	DL Architecture
DMRMTT [6]						-	Low (Order-sensitive)	Maxout + MTT (CNN-based)
Feng et al. [7]	Spatial	Grayscale Image (Spatial Byte Patterns)	Implicit CNN Learning (Black-box)	Spatial Locality	Low (Texture)	Multiple*	Medium (GRU Smoothing)	DSC + GRU (CNN-based)
SLIoTDI [8]						-	Low (Single-session)	LeNet + FGSM (CNN-based)
IoT-SCNet [9]				Spatial Locality (Multi-level)	Medium (Feature Fusion)	Multiple*	Medium (Multi-level)	ResNet-50 (CNN-based)
Proposed Work	Spectral	Spectrograms	Explicit Spectral Features	Multi-resolution Time-frequency, Amplitude, Phase	High (Spectral peaks, Bandwidth)	Only Packet Length	High (Magnitude-invariant)	ViT (Global Self-attention)

* Includes Packet Size, Direction (in/out), Inter-arrival Time, RTT Timing, Protocol Type, TLS/Cipher.

These techniques employed diverse DL approaches to address manual feature engineering and scalability challenges. DMRMTT [6] combines a deep convolutional maxout network with multiple time-series transformers (MTT) to extract spatial and temporal features from 28×28 grayscale fingerprints. Authors in [7] proposed a depth wise separable convolution (DSC) and GRU-based framework using triplet loss for automatic fingerprint extraction from traffic image sequences, enabling fast hierarchical navigable small world (HNSW) searches. SLIoTDI [8] introduced a modular, reusable feature extractor via adversarial training (FGSM) and a joint loss function combining paired, adversarial, and cooperative losses, enabling scalability to unseen devices without retraining. IoT-SCNet [9] leveraged semi-supervised contrastive learning with traffic-specific augmentation strategies to reduce labeled data dependency.

These approaches preserve spatial locality and sequential byte information, but it remains fundamentally limited to amplitude encoding. Additionally, they treat temporal information implicitly where the networks must learn to recognize periodicity, polling cycles, and inter-packet timing patterns through feature extraction rather than explicit frequency decomposition.

C. Proposed Spectral Representation

The fundamental distinction for feature representation between CONTEX-T and existing grayscale image-based approaches lies not only in raw feature extraction, but also in the representational domain and explicit temporal-frequency decomposition. While paper [6], [7], [8], [9] operate in the spatial domain (directly mapping raw packet sequences to pixel intensities), CONTEX-T shifts the entire analytical paradigm to the frequency domain, enabling explicit extraction of periodic device behaviors and spectral signatures that remain hidden in spatial representations. Table I provides comparison of this work with the existing literature for packet representation.

CONTEX-T applies STFT or CWT directly to packet-length sequences, producing spectrograms where spectral peaks correspond to device behaviors like polling cycles and communication patterns. This preserves both temporal (via windowing) and spectral (via FFT) resolution while highlighting discriminative periodic features not visible in spatial representations. The spectral perspective offers several theoretical and practical advantages:

1. *Information-Theoretic Advantage*: For spatial-domain representation G and device identity Y , mutual information $I(Y; G) = H(Y) - H(Y | G)$ captures only first-

order statistics and local spatial correlations. In contrast, spectrograms satisfy $I(Y; S) \geq I(Y; G)$ by explicitly preserving both amplitude (via magnitude spectrum) and phase relationships (via time-frequency localization), encoding device-specific frequencies and temporal modulation patterns invisible to spatial analysis.

2. *Dimensionality and Representation Capacity*: Spatial images map $N = H \cdot W$ bytes bijectively to $H \times W$ pixels with redundant neighboring pixel correlations. Spectrograms instead redistribute information under the constraint of the uncertainty principle $\Delta t \cdot \Delta f \geq \frac{1}{4\pi}$, allowing temporal-frequency resolution trade-offs to be adaptively tuned to signal characteristics. Short windows emphasize fine temporal precision (small Δt) for transient bursts at the expense of frequency resolution, whereas long windows emphasize high frequency resolution (small Δf) for stable polling cycles at the expense of temporal precision.

3. *Interpretability and Expert Correlation*: Spectrograms enable direct visual inspection by domain experts who can correlate frequency signatures with specific device communication protocols, polling cycles, and heartbeat intervals. This provides transparency into which traffic characteristics enable device identification, instead of fully relying on learned representations in a DL black-box.

4. *Multi-Resolution Analysis & Adaptive Trade-offs*: Through tunable STFT window lengths and wavelet scales, spectrograms enable multi-resolution analysis where temporal-frequency resolution can be adaptively adjusted to match deployment scenarios.

5. *Robustness to Jitters and Packet Reordering*: Spatial images are strictly order-sensitive, with CNN activation degradation under packet permutations. Spectrograms exhibit partial shift-invariance due to overlapping STFT windows. A temporal shift induces a phase rotation, but the power spectrum remains translation-invariant in magnitude. CWT provides scale-invariant analysis, where dilation of the signal scales wavelet coefficients predictably. This is a crucial property for networks experiencing variable delays and packet reordering (e.g., Wi-Fi contention, LTE handovers).

III. METHODOLOGY

This section outlines the methodological framework used in the research. We describe the techniques employed to generate spectrogram representations and detail the vision transformer

models integrated into the proposed system.

A. Spectrogram Generation Techniques

To extract discriminative features suitable for DL classification, we transform one-dimensional raw packet sequences into two-dimensional time-frequency spectrograms. This representation simultaneously captures two complementary information dimensions: temporal evolution and frequency content. Time-frequency analysis reveals which frequency components (corresponding to transmission rate patterns) are active at which temporal intervals, enabling neural networks to learn device-specific behavioral signatures that would remain hidden in purely temporal or purely frequency-domain representations.

Let the packet length sequence be denoted as $p = [p_1, p_2, \dots, p_N]$, where $p_n \in \mathbb{R}^+$ represents the length in bytes of the n -th packet and N is the sequence length. The objective is to compute a time-frequency representation $S(t, f)$ that encodes the spectral energy distribution at each temporal location, enabling the extraction of spatially localized features for classification. The fundamental trade-off in time-frequency analysis, formalized by the Heisenberg-Gabor uncertainty principle [22], states that simultaneous perfect localization in both time and frequency is impossible:

$$\Delta t \cdot \Delta f \geq \frac{1}{4\pi}. \quad (1)$$

This principle guides the choice between STFT (fixed resolution) and CWT (adaptive resolution), as both methods represent different strategies for resolving this trade-off.

1) Short-Time Fourier Transform (STFT)

The STFT provides a time-localized frequency decomposition by applying the Fourier transform to windowed segments [23]. Algorithm 1 shows STFT-based spectrogram generation. For a discrete packet sequence $p[n]$, the STFT is:

$$\text{STFT}_m^k = \sum_{n=0}^{R-1} p[m \cdot h + n] \cdot w[n] \cdot e^{-j2\pi kn}, \quad (2)$$

where, m is the time-frame index (indicating which window position), h is the hop size (stride between consecutive windows), $w[n]$ is the window function of length R , k is the frequency bin index, K is the FFT size determined by the window length parameter, and $j = \sqrt{-1}$. We employ the Hann window for its favorable spectral leakage properties that minimize sidelobe leakage [24]:

$$w[n] = 0.5 \left(1 - \cos \left(\frac{2\pi n}{R-1} \right) \right), \quad n = 0, 1, \dots, R-1. \quad (3)$$

The STFT coefficients STFT_m^k are complex-valued. The power spectrum is computed as the magnitude-squared, then converted to decibel scale for perceptual relevance:

$$S_{\text{STFT}}[m, k] = 10 \log_{10}(|\text{STFT}_m^k|^2 + \varepsilon), \quad (4)$$

where $\varepsilon = 10^{-12}$ prevents instability from logarithm of zero.

In STFT, the frequency axis has uniformly spaced bins:

$$f_k = \frac{k \cdot f_s}{K}, \quad (5)$$

where $f_s = 1.0$ cycle/packet (normalized sampling rate). The frequency resolution is:

Algorithm 1: STFT-based Spectrogram Generation

Input: Packet segment $\tilde{p}_i \in \mathbb{R}^{L_{\text{seg}}}$, frequency resolution R , stride f_{stride}

Output: STFT spectrogram $S_{\text{STFT}} \in \mathbb{R}^{T \times (R/2+1)}$

1. Initialize:

- Window length: $L \leftarrow R$
- FFT points: $K \leftarrow R$
- Hop size: $h \leftarrow \lfloor L \cdot f_{\text{stride}} \rfloor$
- Number of frequency bins: $F \leftarrow K/2 + 1$
- Hann: $w[n] \leftarrow 0.5(1 - \cos(2\pi n/(R-1)))$ for $n = 0, \dots, R-1$
- Sampling rate: $f_s \leftarrow 1.0$ cycle/packet
- Frequency axis: $f[k] \leftarrow (k \cdot f_s)/K = k/R$ for $k = 0, 1, \dots, F-1$
- Number of frames: $T \leftarrow \lfloor (L_{\text{seg}} - R)/h \rfloor + 1$

2. Compute STFT:

- for $m = 0$ to $T-1$ do
 - for $k = 0$ to $F-1$ do
 - $\text{STFT}[m, k] \leftarrow \sum_{n=0}^{R-1} \tilde{p}_i[m \cdot h + n] \cdot w[n] \cdot e^{-j2\pi kn/K}$
 - end for
- end for

3. Convert to Spectrogram:

- for $m = 0$ to $T-1$ do
 - for $k = 0$ to $F-1$ do
 - $S_{\text{STFT}}[m, k] \leftarrow 10 \log_{10}(|\text{STFT}[m, k]|^2 + 10^{-12})$
 - end for
- end for

4. Return $S_{\text{STFT}} \in \mathbb{R}^{T \times (R/2+1)}$

$$\Delta f = \frac{f_s}{R}, \quad (6)$$

where R is the window length parameter. In the implementation, the spectral resolution parameter $R \in \{16, 32, 64\}$ determines the window length (with $K = R$), yielding three spectral resolution levels: $R = 16$ for coarse frequency resolution $\Delta f = 1/16$ and fine temporal resolution $\Delta t = 16$ packets; $R = 32$ for medium resolution in both domains; and $R = 64$ for fine frequency resolution $\Delta f = 1/64$ and coarse temporal resolution $\Delta t = 64$ packets.

The limitation of STFT is its fixed time-frequency resolution. A window of length R determines both temporal and frequency localization with inverse relationship $\Delta t \cdot \Delta f = 1$, which cannot be separately optimized. Increasing R improves frequency resolution but worsens temporal resolution, preventing accurate simultaneous localization of transient events and narrow frequency components. This uniform trade-off applies identically across all frequencies, making STFT particularly effective for stationary signals but less suitable for highly non-stationary traffic patterns.

2) Continuous Wavelet Transform (CWT)

CWT circumvents the STFT resolution limitation through scale-dependent analysis. Algorithm 2 shows CWT-based spectrogram generation. Instead of a fixed window, the CWT uses scaled and translated copies of a single mother wavelet function [25], [26]:

$$W(a, b) = \frac{1}{\sqrt{a}} \int_{-\infty}^{\infty} p(t) \cdot \bar{\psi} \left(\frac{t-b}{a} \right) dt, \quad (7)$$

Where, $a \in \mathbb{R}^+$ is the scale parameter (small scales correspond to high frequencies, large scales correspond to low frequencies), $b \in \mathbb{R}$ is the translation parameter (temporal localization), $\psi(t)$ is the mother wavelet function and $\bar{\psi}$ denotes the complex conjugate.

Algorithm 2: CWT-based Spectrogram Generation

Input: Packet segment $\tilde{\mathbf{p}}_i \in \mathbb{R}^{L_{\text{seg}}}$, frequency resolution R ,

Output: CWT spectrogram $S_{\text{CWT}} \in \mathbb{R}^{R \times L_{\text{seg}}}$

1. **Initialize:**

- Number of scales: $N_s \leftarrow R$
- Morlet wavelet center frequency: f_c
- Sampling rate: $f_s \leftarrow 1.0$ cycle/packet
- Frequency bounds:
 - $f_{\min} \leftarrow f_s/(2R) = 1/(2R)$ (minimum resolvable frequency)
 - $f_{\max} \leftarrow f_s/2 = 0.5$ (Nyquist frequency)
- Numerical stability constant: $\varepsilon \leftarrow 10^{-12}$

2. **Generate Logarithmically-spaced Frequency and Scale Arrays:**

- for $i = 0$ to $N_s - 1$ do
 - $f[i] \leftarrow f_{\min} \cdot \left(\frac{f_{\max}}{f_{\min}}\right)^{i/(N_s-1)}$
 - $s[i] \leftarrow \frac{f_c \cdot f_s}{f[i]} = \frac{0.8125}{f[i]}$
- end for
- Note: This creates R scales ordered from largest (index $j=0$, lowest frequency) to smallest (index $j=R-1$, highest frequency)

3. **Compute CWT:**

- for $j = 0$ to $N_s - 1$ do
 - for $n = 0$ to $L_{\text{seg}} - 1$ do
 - Compute: $W[j, n] \leftarrow \frac{1}{\sqrt{s[j]}} \sum_{n'=0}^{L_{\text{seg}}-1} \tilde{\mathbf{p}}_i[n'] \cdot \bar{\psi}\left(\frac{n'-n}{s[j]}\right)$
 - end for
- end for

4. **Convert to Spectrogram:**

- for $j = 0$ to $N_s - 1$ do
 - for $n = 0$ to $L_{\text{seg}} - 1$ do
 - $S_{\text{CWT}}[j, n] \leftarrow 10\log_{10}(|W[j, n]|^2 + 10^{-12})$
 - end for
- end for

5. **Return $S_{\text{CWT}} \in \mathbb{R}^{R \times L_{\text{seg}}}$**

For discrete implementation with packet sequences, we define the spectral resolution $R \in \{16, 32, 64\}$ as the number of scales at which the CWT is evaluated. The discrete scales $\{s_j\}_{j=1}^R$ are derived from R logarithmically spaced frequencies $\{f_j\}_{j=1}^R$ between f_{\min} and f_{\max} via:

$$s_j = \frac{f_c \cdot f_s}{f_j}, j = 1, 2, \dots, R, \quad (8)$$

where f_c is the center frequency of the Morlet wavelet and $f_s = 1.0$ is the sampling rate (cycles/packet). CWT's defining characteristic is its adaptive resolution. Each scale corresponds to a pseudo-frequency through equation (8). This mapping creates multi-resolution analysis. High frequencies (small scales) create fine temporal resolution, coarse frequency resolution and low frequencies (large scales) create coarse temporal resolution, fine frequency resolution.

The discrete CWT is then computed as:

$$W[j, n] = \frac{1}{\sqrt{s_j}} \sum_{n'=0}^{N-1} p[n'] \cdot \bar{\psi}\left(\frac{n'-n}{s_j}\right), j = 1, 2, \dots, R, \quad (9)$$

where the sum is over the packet indices. We employ the complex Morlet wavelet with a center frequency of f_c cycles/sample (normalized frequency). This is a standard implementation used in widely deployed signal processing libraries for computational consistency. The Morlet wavelet combines sinusoidal oscillation with a Gaussian envelope, providing excellent joint localization in both time and

frequency domains. This makes it well-suited for detecting transient packet rate changes superimposed on sustained background traffic patterns [25], [27]. The CWT power spectrogram is converted to decibel:

$$S_{\text{CWT}}[j, n] = 10 \log_{10} (|W[j, n]|^2 + \varepsilon). \quad (10)$$

Formally, the time-frequency resolution cells have area proportional to frequency:

$$\Delta t(f) \cdot \Delta f(f) = \frac{\Delta t_0}{f} \cdot \Delta f_0 \cdot f = \Delta t_0 \cdot \Delta f_0 = \text{constant}. \quad (11)$$

This means CWT achieves better frequency resolution at low frequencies (useful for sustained traffic patterns) and better time resolution at high frequencies (useful for burst detection). Additionally, CWT provides multiresolution analysis where resolution varies with frequency as opposed to STFT which maintains constant time-frequency resolution across all frequencies [28], [29]. We use the same three spectral resolution levels $R \in \{16, 32, 64\}$ for CWT as for STFT, where R controls the number of frequency points in the analyzed range. This enables fair comparison of device classification accuracy across both transformation methods.

B. Vision Transformer Models

This research employs three state-of-the-art vision transformer (ViT) architectures for classifying IoT devices based on their spectrogram representations. DeiT-Base (data-efficient image transformer - base) [30], ViT-Small (vision transformer - small) [31] and EfficientViT-B1 (efficient vision transformer - base variant 1) [32]. The ViT processes input images through a sequence of operations that transform 2D spatial data into a 1D sequence of embeddings suitable for transformer processing [33], [34]. It partitions input spectrograms $X \in \mathbb{R}^{H \times W \times C}$ into non-overlapping patches of size $P \times P$ pixels. For standardized input size $H = W = 224$ and $C = 3$ (RGB), the image yields $N = \frac{H \cdot W}{P^2} = \frac{224 \times 224}{16^2} = 196$ patches. Each patch $x_i \in \mathbb{R}^{P^2 \cdot C}$ is linearized and projected to a d -dimensional embedding space:

$$z_i = E \cdot \text{vec}(x_i) + b_e, \quad (12)$$

where $E \in \mathbb{R}^{d \times P^2 \cdot C}$ is the patch embedding matrix, $\text{vec}(x_i)$ is the vectorized patch, and $b_e \in \mathbb{R}^d$ is the embedding bias. Learnable position embeddings $p_i \in \mathbb{R}^d$ encode spatial location information:

$$z_i^{\text{pos}} = z_i + p_i. \quad (13)$$

A learnable class token $z_{\text{cls}} \in \mathbb{R}^d$ is prepended to the sequence of $N + 1 = 197$ tokens:

$$Z^{(0)} = [z_{\text{cls}}; z_1^{\text{pos}}; \dots; z_N^{\text{pos}}] \in \mathbb{R}^{(N+1) \times d}. \quad (14)$$

This sequence is processed through L transformer encoder layers. Each layer l applies multi-head self-attention (MSA) with residual connection:

$$A^{(l)} = \text{MSA}(\text{LN}(Z^{(l-1)})), \quad (15)$$

$$Z'^{(l)} = Z^{(l-1)} + A^{(l)}, \quad (16)$$

followed by a feed-forward network (FFN):

$$F^{(l)} = \text{FFN}(\text{LN}(Z'^{(l)})), \quad (17)$$

$$Z^{(l)} = Z'^{(l)} + F^{(l)}, \quad (18)$$

where $l \in \{0, 1, \dots, L\}$, with $l = 0$ representing the input token

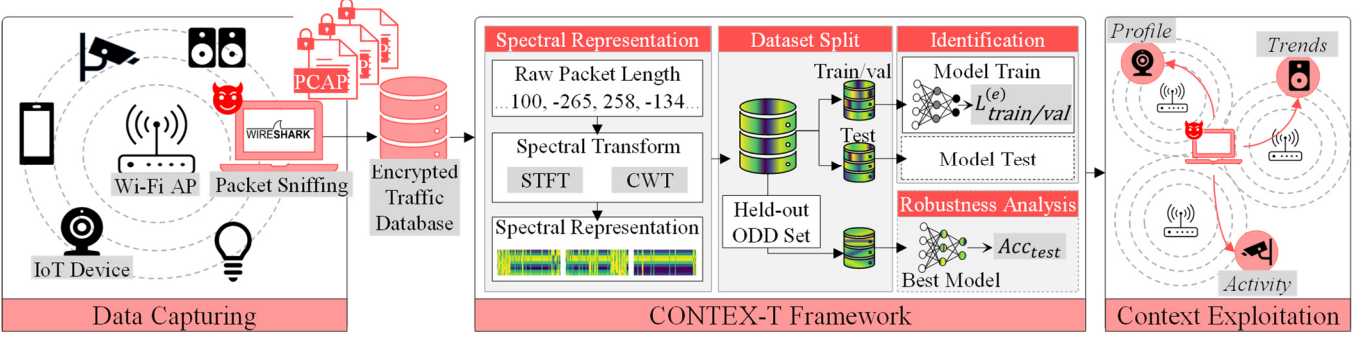


Fig. 1. Overview of the proposed framework.

sequence and $l = L$ representing the final transformed representation. LN denotes layer normalization. Multi-head attention with H heads computes:

$$\text{Attention}(Q, K, V) = \text{softmax}\left(\frac{QK^T}{\sqrt{d_k}}\right)V, \quad (19)$$

with $d_k = d/H$ per head. After L layers, the class token embedding $z_{\text{cls}}^{(L)}$ is extracted and passes a classification head:

$$\hat{y} = \text{softmax}(W_{\text{head}}z_{\text{cls}}^{(L)} + b_{\text{head}}), \quad (20)$$

$$d_{\text{pred}} = \arg \max_c \hat{y}_c, \quad (21)$$

where $W_{\text{head}} \in \mathbb{R}^{|D| \times d}$ and $|D| = 14$ device classes.

IV. THREAT MODEL AND SYSTEM DESIGN

This section presents the adversarial threat model considered in this work and explains how it informs the overall system architecture. We also describe the design principles and components of the proposed system.

A. Adversarial Threat Model

The adversary, denoted \mathcal{A} , is modeled as a passive eavesdropper operating under the honest-but-curious paradigm. Fig. 1 illustrates the overview of the adversarial framework. The adversary captures packet metadata via wireless sniffing but does not modify, inject, or probe network traffic. Formally, the adversary has GPU-accelerated inference capabilities, access to training samples per device ($|T_{\text{train}}^{(d)}|$), knowledge of the device class set D and the model f_{θ} , and access to general signal processing priors. This can be formally expressed:

$$\mathcal{A} \left\{ \text{inference}, |T_{\text{train}}^{(d)}|, \text{knowledge of } D, f_{\theta}, \text{ and signal priors} \right\}. \quad (22)$$

Although computationally capable, the adversary is subject to several critical constraints that define the threat model's scope. First, the payload confidentiality constraint ensures that encrypted application-layer content cannot be inspected, restricting the adversary's inference to observable metadata, specifically packet lengths. This is a fundamental assumption in traffic analysis attacks, where cryptography protects semantic content but not its structure or volume. Second, the strict passivity constraint prohibits the adversary from actively interacting with the network, including packet injections, timing manipulation, or protocol-level probing. The adversary can only observe traffic and does not have the capability to modify network conditions or inject false data. Third, the temporal boundedness constraint limits the adversary's training process to a fixed reconnaissance period

during which the target network is observable. No adaptive retraining is possible during deployment, which may degrade classification accuracy under non-stationary traffic conditions where packet size distributions evolve over time. Fourth, the limited protocol visibility constraint prevents the adversary from achieving full recovery of higher-layer semantics; the adversary cannot decrypt application-level protocols or infer fine-grained behavioral details, limiting the threat scope to device identification from observable traffic patterns.

Adversarial Objectives and Success Metrics: An adversarial identification attack is considered successful if the test-set accuracy exceeds $\text{Acc}_{\text{test}} \geq 90\%$ with a bootstrap confidence interval width $\Delta_{\text{CI}} < 5\%$, where:

$$\text{Acc}_{\text{test}} = \left(\frac{1}{N_{\text{test}}} \sum_{i=1}^{N_{\text{test}}} \mathbf{1}[\hat{y}_i = y_i] \right) \times 100\%, \quad (23)$$

with N_{test} = test samples across 14 devices. This significantly exceeds the random-guessing baseline of $1/|D| \approx 7.14\%$ for 14-way classification. The confidence interval requirement ensures that the success claim is statistically robust and not due to random variation in the test set.

Beyond the primary success criterion, the adversary pursues several secondary objectives to ensure robust and reliable device identification across operational conditions. Cross-configuration robustness measures whether the attack maintains consistent performance across all 24 experimental configurations (combinations of transformation method, spectral resolution, segment length, and overlap). This is quantified by minimizing the accuracy variance:

$$\min_{c_1, c_2 \in \mathcal{C}} |\text{Acc}_{\text{test}}(c_1) - \text{Acc}_{\text{test}}(c_2)| \approx 0. \quad (24)$$

This ensures that the attack is not sensitive to the specific spectrogram generation parameters and remains effective regardless of which transformation or resolution is employed. Balanced per-class performance ensures that device classification accuracy is not biased toward certain devices, which could be exploited for defense. This is measured using the weighted F1-score across all device classes:

$$\text{Weighted } F_1 = \frac{1}{|D|} \sum_{d \in D} w_d F_1^{(d)} \geq 0.90, \quad (25)$$

where w_d is the weight for device d (proportional to the number of test samples for that device), and $F_1^{(d)}$ is the F1-score for device d . A high weighted F1-score indicates that the adversary can accurately identify all device types. Invariance to segmentation parameters captures whether classification accuracy remains stable across different segment lengths $L_{\text{seg}} \in$

{100,500}, and overlap $p_{overlap} \in \{0\%, 50\%\}$:

$$Acc_{test}(L_{seg}, p_{overlap}) \approx \text{constant}. \quad (26)$$

This ensures that the attack generalizes regardless of how packet sequences are segmented for analysis.

B. System Design

1) Heterogeneous IoT Traffic Representation

We consider a heterogeneous internet of things (IoT) network composed of $|D| = 14$ distinct device types communicating over encrypted channels. While application-layer payloads are protected by cryptographic mechanisms, packet-level metadata, specifically packet lengths remain observable in plaintext within network layers to support routing and link-layer operations. The traffic of each device $d \in D$ is modeled as a temporal sequence of packet lengths:

$$p_d = [p_{d,1}, p_{d,2}, \dots, p_{d,T_d}], p_{d,i} \in \mathbb{Z}^+, \quad (27)$$

where $p_{d,i}$ denotes the length in bytes of the i -th packet emitted by device d . For subsequent analysis, each traffic stream is partitioned into windows of fixed size $N = 1000$ packets, producing a collection of segments:

$$p_d^{(r)} = [p_{d,r,1}, p_{d,r,2}, \dots, p_{d,r,N}] \in \mathbb{Z}_+^N, \quad (28)$$

where r indexes the window position within the device's trace. The segmentation process optionally incorporates partial overlap between consecutive windows, parameterized by $L_{seg} \in \{100, 500\}$ and $p_{overlap} \in \{0\%, 50\%\}$.

To generate multiple training examples from raw packet sequences while preserving local temporal patterns, we apply sliding window segmentation. Given a full packet sequence p of length N , we extract overlapping segments of length L_{seg} :

$$p_i = [p[i \cdot s_{stride}], p[i \cdot s_{stride} + 1], \dots, p[i \cdot s_{stride} + L_{seg} - 1]], \quad (29)$$

where $i = 0, 1, \dots, \lfloor (N - L_{seg})/s_{stride} \rfloor$ is the segment index. The stride is determined by the desired overlap percentage:

$$s_{stride} = L_{seg} \cdot (1 - p_{overlap}), \quad (30)$$

where $p_{overlap} \in \{0\%, 50\%\}$ specifies 0% (non-overlapping) or 50% (50% overlap) configurations. The relationship between stride and overlap is: $s_{stride} = 1 - p_{overlap}$. For example, with $L_{seg} = 100$ packets and $p_{overlap} = 0.5$ (50% overlap): $s_{stride} = 100 \cdot (1 - 0.5) = 50$ packets, meaning consecutive segments begin 50 packets apart, creating 50% overlap between adjacent segments.

This windowing strategy achieves a balance between temporal resolution and local stationarity, a property required for subsequent spectral transformations. Overlapping windows create smoother temporal transitions in the spectrogram sequence, capturing behavioral signatures that might be lost at segment boundaries. Additionally, overlapping generates more training samples without requiring additional data collection, which is critical for DL models that benefit from larger training sets while mitigating overfitting risks.

2) Feature Extraction and Classification Pipeline

Each traffic segment $p_d^{(r)}$ undergoes a five-stage feature extraction and classification pipeline. Stage 1 is reprocessing and mean-centering, defined as:

$$\tilde{p}_d^{(r)} = p_d^{(r)} - \mu_d, \text{ where } \mu_d = \frac{1}{N} \sum_{i=1}^N p_{d,r,i}. \quad (31)$$

This step removes device-specific bias in packet size distributions while preserving relative variations. The second stage applies a time-frequency transformation, denoted as:

$$T(\tilde{p}_d^{(r)}) = \begin{cases} \text{STFT}(\tilde{p}_d^{(r)}; R), & \text{if using STFT} \\ \text{CWT}(\tilde{p}_d^{(r)}; R), & \text{if using CWT} \end{cases} \quad (32)$$

where the parameter $R \in \{16, 32, 64\}$ controls the spectral resolution (number of frequency bins). The choice of transformation (STFT vs CWT) is fixed for each experimental configuration. Stage 3 is device-specific percentile-based normalization: After transforming to the spectral domain, spectrograms exhibit device-specific value distributions. For each device d , normalization parameters are computed independently using only the training spectrogram samples:

$$v_{min} = \text{percentile}_5(\{S_i^{(d)} : i \in M_{train}\}), \quad (33)$$

$$v_{max} = \text{percentile}_{95}(\{S_i^{(d)} : i \in M_{train}\}), \quad (34)$$

where M_{train} is the number of training spectrograms for device d and $S_i^{(d)}$ represents the spectrogram for training sample i of device d . These normalization parameters are computed exclusively from training data and applied identically to both training and test sets to prevent data leakage. The resulting normalized spectrogram is computed as:

$$\hat{S}_d^{(r)} = \frac{S_d^{(r)} - v_{min}}{v_{max} - v_{min}}, \quad (35)$$

where v_{min} and v_{max} denote the 5th and 95th percentile intensity values for device d computed from the training spectrogram samples. Values outside the 5th–95th percentile range are clipped to preserve signal integrity. This percentile-based approach concentrates dynamic range on typical spectral patterns (inner 90% of values), reduces sensitivity to outlier traffic anomalies in normalization, enables fair comparison across devices with different traffic volumes and maintains data integrity by using only training statistics. These device-specific normalization parameters v_{min}^d , v_{max}^d are derived from the training data and are applied consistently to prevent temporal position leakage while ensuring test data uses the same normalization as training data for that device. Stage 4 encodes the normalized spectrogram into a visual format by resizing it to 224×224 pixels and mapping it to a three-channel RGB representation:

$$X_{d,r} = \text{ResizeRGB}(\hat{S}_d^{(r)}, 224 \times 224). \quad (36)$$

Finally, the fifth stage performs device classification using a pretrained ViT model $f_\theta(\cdot)$, producing a probability vector:

$$y_{d,r} = f_\theta(X_{d,r}) \in [1]^{ID|}, \sum_{c=1}^{ID|} y_{d,r,c} = 1, \quad (37)$$

from which the predicted device label is obtained as:

$$d_{pred}^{(r)} = \arg \max_{c \in D} y_{d,r,c}. \quad (38)$$

3) Training Configuration

The training pipeline follows a specific sequence: (1) data is first partitioned into training, validation, and test sets with per-device seeding for reproducibility, (2) normalization statistics are computed exclusively from the training set, (3) the training

set undergoes sequential augmentation while validation and test sets do not, (4) the model is optimized using the specified learning rate schedule, and (5) training executes in epochs with early stopping. This structured approach ensures that model development is isolated from evaluation data, preventing data leakage and enabling honest assessment of model performance. Summary of DL and training configuration is given in Table II.

Dataset Partitioning and Normalization: From the available spectrograms generated from the raw packet lengths per device, training, validation and test set are created via a randomized device-specific split that would be detailed in section V.A. Reproducibility is ensured through seeded random number generation which guarantees deterministic and reproducible partitioning across runs and environments.

Instead of using standard ImageNet normalization, dataset-specific statistics are computed exclusively from the training spectrograms. For each channel $c \in \{R, G, B\}$, the mean $\mu_c \in \mathbb{R}$ and standard deviation $\sigma_c \in \mathbb{R}$ are calculated as:

$$\mu_c = \frac{1}{N_{\text{train}}} \sum_{i=1}^{N_{\text{train}}} \frac{1}{H \cdot W} \sum_{h,w} X_i^{(h,w,c)}, \quad (39)$$

$$\sigma_c = \sqrt{\frac{1}{N_{\text{train}}} \sum_{i=1}^{N_{\text{train}}} \frac{1}{H \cdot W} \sum_{h,w} (X_i^{(h,w,c)} - \mu_c)^2}. \quad (40)$$

Each spectrogram image is then normalized per channel:

$$\tilde{X}_c^{(h,w)} = \frac{X_c^{(h,w)} - \mu_c}{\sigma_c}, c \in \{R, G, B\}. \quad (41)$$

This normalization ensures zero-mean, unit-variance inputs, which improves training convergence and overall model performance. After computing normalization statistics from the training set, augmentation is applied exclusively to training spectrograms. Validation and test sets receive only resizing and per-channel normalization (using the training-computed statistics) for unbiased evaluation, ensuring that augmentation effects do not confound downstream evaluation metrics.

Training Procedure and Early Stopping: The model is trained using cross-entropy loss with label smoothing $\alpha = 0.1$:

$$L_{\text{CE}} = - \sum_{c=1}^{|D|} \tilde{y}_c \log(\hat{y}_c), \quad (42)$$

where $\tilde{y}_c = (1 - \alpha)\delta(c, y) + \alpha/|D|$ is the smoothed label distribution, and $\delta(c, y) = 1$ if $c = y$, otherwise $\delta(c, y) = 0$. The training configuration includes batch size $B = 16$, maximum epochs $E_{\text{max}} = 50$, gradient clipping where the gradient norm $\|\nabla_{\theta} L\|_2$ is clipped to a maximum of 1.0 to prevent exploding gradients during backpropagation and early stopping. For each epoch $e \in \{1, \dots, E_{\text{max}}\}$ training loss and accuracy are computed as:

$$L_{\text{train/val}}^{(e)} = \frac{1}{N_{\text{train/val}}} \sum_{(X,y) \in \mathcal{D}_{\text{train/val}}} L_{\text{CE}}(\text{softmax}(f_{\theta}(X)), \tilde{y}), \quad (43)$$

$$\text{Acc}_{\text{train/val}}^{(e)} = \frac{1}{N_{\text{train/val}}} \sum_{(X,y) \in \mathcal{D}_{\text{train/val}}} \mathbf{1}[\arg \max f_{\theta}(X) = y]. \quad (44)$$

When measuring validation loss y is used instead of \tilde{y} in (43)

TABLE II
SUMMARY OF DL AND TRAINING CONFIGURATION

DL Configuration	Specification
	1. DeiT-Base • Parameters (~86M), Dimension (768) • Transform Layer (12), Attention Head (12) • Transfer: ImageNet + knowledge Distillation
DL Architecture:	2. ViT Small • Parameters (~22M), Dimension (384) • Transform Layer (12), Attention Head (6) • Transfer : ImageNet
	3. EfficientViT-B1 • Parameters (~7M) Dimension (256) • Transform Layer (4), Attention Head (4) • Transfer: ImageNet, Efficient Attention
Input Specification:	PNG, 224x224 pixels, 3 channel (RGB)
Learning Rate:	1×10^{-4} , Scheduler (OneCycleLR)
Optimizer:	AdamW, Adam Parameter (β_1, β_2) (0.9, 0.999)
Weight Decay:	L2 Regularization (0.05)
Gradient Clipping:	Max Norm (1.0)
Loss Function:	CrossEntropyLoss
Augmentation:	• Random Horizontal Flip (0.5) • Random Vertical Flip (0.3) • Random Affine Transform: Degrees ($\pm 5^\circ$), Translation ($\pm 10\%$), Scale (0.9–1.1) • Color Jitter: Brightness and Contrast (± 0.2) • Gaussian Blur: 3×3 (kernel), $\sigma \in [0.1, 0.5]$

and vice versa for accuracy in (43) (without gradient computation). Training terminates early if $\text{Acc}_{\text{val}}^{(e)}$ does not improve for $P = 15$ consecutive epochs. This configuration balances computational efficiency, convergence speed, and generalization performance across the three ViT architectures.

V. RESULTS AND DISCUSSION

This section reports the experimental findings obtained from the evaluation. We analyze traffic characteristics, assess DL performance and examine robustness of the system.

A. Experimental Configuration

The experimental design explores the factorial combination of transformation method, spectral resolution, segment length, and overlap fraction. Formally:

$$|\mathcal{C}| = 2_{(\text{STFT/CWT})} \times 3_R \times 2_{(L_{\text{seg}})} \times 2_{(p_{\text{overlap}})}, \quad (45)$$

where 2 transformation methods of STFT vs CWT, 3 spectral resolutions: $R \in \{16, 32, 64\}$, 2 segment lengths $L_{\text{seg}} \in \{100, 500\}$ packets and 2 overlap levels $p_{\text{overlap}} \in \{0\%, 50\%\}$, total 24 configurations. This comprehensive factorial design enables systematic evaluation of how each hyperparameter affects device identification accuracy and robustness.

Dataset: For the experiments, we used the UNSW IoT Traffic Dataset [17] as the data source. The dataset comprises network traffic from a range of IoT devices operating under diverse configurations. As the objective of this work is to analyze packet length characteristics of encrypted wireless traffic across heterogeneous devices, the selection of devices (listed in Table III) was made to ensure diversity and sufficient data availability for each type. To enable reliable model development and evaluation, the dataset was systematically divided into training, validation, and testing subsets across the 24 experimental configurations, as summarized in Table IV.

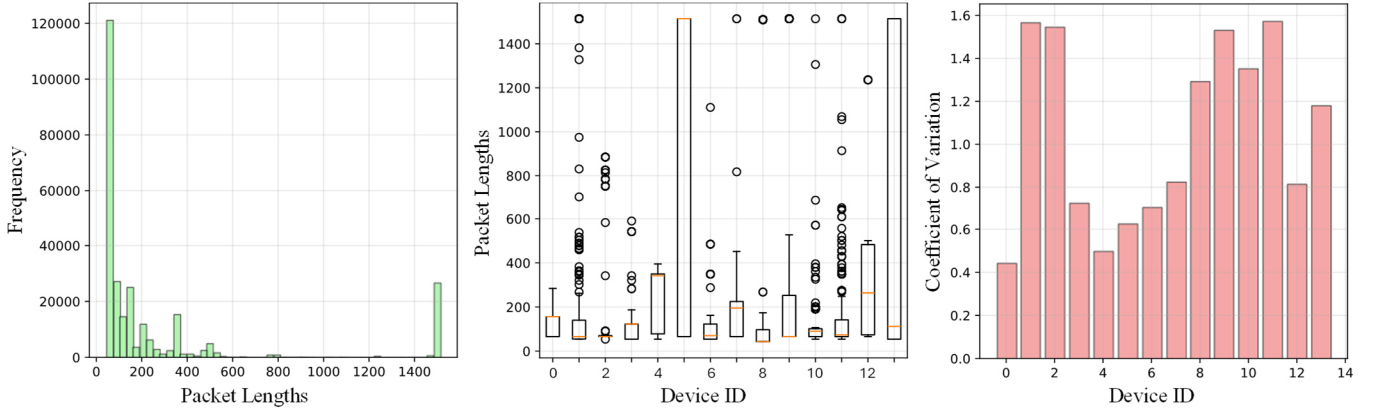


Fig. 2. Packet statistics of the devices in the dataset.

TABLE III

PER-DEVICE PACKET STATISTICS

Dev	Name	MAC	μ	σ
0	Dropcam	30:8c:fb:2f:e4:b2	113.1	50.2
1	HP Printer	70:5a:0f:e4:9b:c0	151.7	237.9
2	Triby Speaker	18:b7:9e:02:20:44	143.7	222.5
3	Light Bulbs LiFX Smart Bulb	d0:73:d5:01:83:08	109.8	79.9
4	Netatmo Weather Station	70:ee:50:03:b8:ac	258.1	128.9
5	Nest Dropcam	30:8c:fb:b6:ea:45	1057.6	663.3
6	TP-Link Day Night Camera	f4:f2:6d:93:51:f1	106.8	75.6
7	Withings Aura Sleep Sensor	00:24:e4:20:28:c6	167.7	138.6
8	Netatmo Welcome	70:ee:50:18:34:43	499.0	645.9
9	Belkin Wemo Switch	ec:1a:59:79:f4:89	277.1	424.7
10	Amazon Echo	44:65:0d:56:cc:d3	124.3	168.2
11	Samsung Galaxy Tab	08:21:ef:3b:fcc:3	211.5	333.0
12	Samsung SmartCam	00:16:6c:ab:6b:88	293.1	239.0
13	MacBook	ac:bc:32:d4:6f:2f	519.2	613.6

B. Traffic Analysis

Packet Statistics: The 14 IoT and consumer devices in the dataset demonstrate significant heterogeneity in packet size distributions, attributable to their diverse communication protocols and distinct traffic behaviors that form the basis for device-specific fingerprinting. Table III and Fig. 2 summarize the packet-length statistics of each device which were generated from over 20,000 packets per device, with statistical descriptors such as mean (μ), standard deviation (σ) and coefficient of variation (cv) computed to capture both the central tendency and variability of transmitted packet lengths. Devices such as dropcam, LiFX smart bulb, Netatmo weather station, Nest dropcam, TP-Link camera, Withings sleep sensor and Samsung SmartCam exhibit relatively low variability ($cv \leq 0.8$), reflecting stable and periodic traffic patterns typical of sensing or monitoring applications. In contrast, devices like the HP Printer, Triby Speaker, Netatmo Welcome, Belkin Wemo Switch, Amazon Echo, Samsung Galaxy Tab, and MacBook show high variability ($cv \geq 1.0$), suggesting bursty or mixed interactive traffic driven by user activity, multimedia streaming, or dynamic network exchanges. The Nest Dropcam stands out with the highest mean packet length (≈ 1058 bytes) and high variability. All devices show minimum packet sizes around 43–66 bytes, corresponding to wireless control or acknowledgment frames and maximum values near 1500 bytes, reflecting the upper bound of standard IP-layer packet sizes in wireless

TABLE IV
TRAIN, VALIDATION AND TEST SPLIT

L_{seg}	p_{overlap}	R	Train Set		Val set		Test set	
			Pkts	Images	Pkts	Images	Pkts	Images
100	0%	100	40000	400	8000	80	8000	80
	50%		20000	400	4000	80	4000	80
	0%	{16,32,64}	75000	150	1500	30	1500	30
	50%		37500	150	750	30	750	30

networks. This inter-device heterogeneity in packet-size dynamics demonstrates that packet-length statistics encode robust, discriminative, and non-payload-dependent device signatures suitable for accurate IoT device fingerprinting.

Spectral Visual Inspection: Fig. 3 illustrates a sample spectral representation of device (0) (dropcam). For STFT, at coarse spectral resolution ($R = 16$), both $L_{\text{seg}} = 100$ and $L_{\text{seg}} = 500$ spectrograms exhibit dominant vertical color bands encoding periodic energy in specific frequency bins correspond to short-term periodic bursts in packet transmission. At intermediate resolution ($R = 32$), the vertical bands subdivide into finer striations, and color gradations from dark teal to bright green become visible, representing packet-length variations around the mean. As resolution increases ($R = 64$), these structures become smoother and more continuous, capturing finer temporal variations and subtle frequency modulations within the shorter observation window. In contrast, spectrograms generated with $L_{\text{seg}} = 500$ reveal markedly richer temporal dynamics and denser vertical striping, reflecting the extended observation window's ability to capture more long-term fluctuations in packet-size behavior. The higher segment length also increases spectral density, allowing the persistence and periodicity of transmission bursts to emerge more clearly, particularly at lower resolutions ($R = 16, 32$), while the highest resolution ($R = 64$) captures both fine-grained temporal variability and background continuity.

CWT spectrograms illustrate hierarchical arc-like interference patterns. The $L_{\text{seg}} = 100$ spectrograms display pronounced arc-like patterns, while $L_{\text{seg}} = 500$ spectrograms show these patterns extended across the full temporal span, indicating that wavelet scales are dynamically distributed across the longer duration. As resolution increases from $R = 16$ to $R = 64$, the wavelet coefficients become progressively finer, revealing more detailed oscillatory contours and multi-

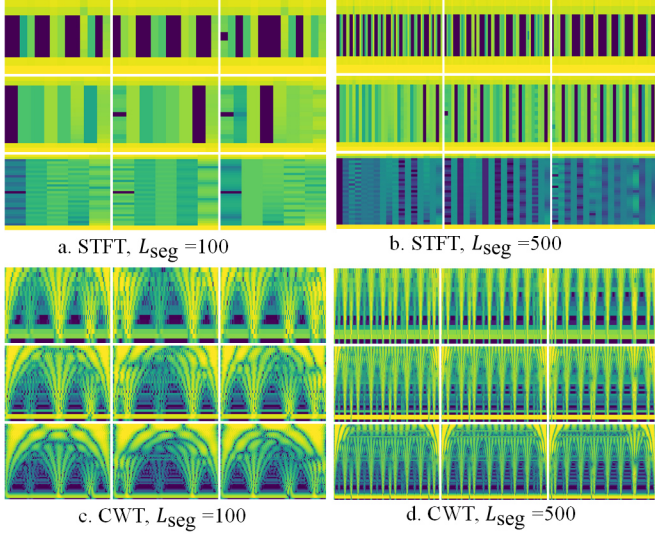


Fig. 3. Sample spectrogram of Device (0). The spectral resolutions $R \in \{16, 32, 64\}$ from top to bottom, respectively.

scale harmonics that highlight device-specific periodicities and transient bursts. The patterns arc-like subdivide into nested sub-patterns with fine striations interleaved within the gradients, capturing scale-dependent spectral features at multiple resolutions simultaneously. $L_{seg} = 100$ and $L_{seg} = 500$ spectrograms exhibit visually distinct patterns, $L_{seg} = 500$ displays finer, more densely packed striations, while $L_{seg} = 100$ shows coarser sub-patterns concentrated in narrower frequency bands. At the finest resolution ($R = 64$), rich multi-scale texture dominates, where $L_{seg} = 100$ concentrates detail in mid-frequency regions (consistent with the device's stable 109-byte median), while $L_{seg} = 500$ extends energy across the full frequency range including ultra-low frequencies. This captures extended low-frequency periodicities spanning hundreds of packets that cannot be represented in brief 100-packet windows. Overall, increasing L_{seg} expands temporal coverage, while increasing R refines frequency precision as CWT can encode both transient and sustained traffic behaviors.

C. DL Evaluation

The primary goal of CONTEX-T is to evaluate how well advanced DL architectures can exploit the information encoded in spectrograms for IoT device identification. Three transformer-based models (DeiT-Base, ViT-Small, and EfficientViT) were systematically compared across the 24 configurations. Table V presents the model performance.

Across all configurations and model architectures, the models consistently demonstrated superior performance. For STFT-based spectrograms, test accuracy typically exceeded 98% (as shown by green-highlighted cells in the table). The best performance for short segments ($L_{seg} = 100, R = 16, p_{overlap} = 0\%$) was achieved by DeiT-Base, with 98.57% accuracy and an F1-score of 0.9857. Accuracy improved on longer segments, exceeding 99%. With $p_{overlap} = 50\%$, performance improved further for both segment lengths, achieving best accuracy with low resolution ($R = 16$).

CWT-based spectrograms showed comparable or slightly better results, especially at higher resolutions ($R = 32, 64$) and longer segments ($L_{seg} = 500$). The highest test accuracy of 100% (F1 = 1) was achieved by EfficientViT and ViT-Small for $L_{seg} = 500$ and $R = 32, 64$ with $p_{overlap} = 50\%$. Even for shorter segments ($L_{seg} = 100$), CWT models maintained exceptional performance, with F1-scores up to 0.9946 and minimal variance, confirming the robustness and precision of spectral representations for device identification.

Impact of Segment Length, Resolution, and Overlap: Increasing the segment length from 100 to 500 packets greatly enhanced performance stability, as longer segments capture richer temporal and spectral features that reveal device-specific periodicities and burst patterns. Both STFT and CWT achieved their best results at $L_{seg} = 500$. Lower spectral resolution ($R = 16$) performed particularly well for STFT, while intermediate resolutions ($R = 32$) offered the best balance between accuracy and generalization. At the highest resolution ($R = 64$), CWT models sometimes achieved perfect performance, though STFT results slightly declined due to sensitivity to fine frequency variations. Additionally, applying a 50% overlap increased sample diversity and temporal context, consistently yielding modest improvements in accuracy and F1 by enhancing robustness to minor temporal shifts.

Model Comparison: Among the ViT variants, DeiT-Base generally achieved the highest performance across both STFT and CWT, particularly for moderate or longer L_{seg} and higher $p_{overlap}$. EfficientViT also matched or outperformed DeiT-Base in CWT configurations, showing that lightweight transformer designs do not compromise accuracy when spectral features are used. ViT-Small achieved strong results but lagged DeiT-Base and EfficientViT in more challenging or lower-resolution scenarios, likely due to its reduced model capacity. Notably, in several CWT configurations ($L_{seg} = 500, R = 32, 64, p_{overlap} = 50\%$), both EfficientViT and ViT-Small achieved perfect F1-scores (F1 = 1) with 100% accuracy and zero confidence interval, indicating complete separability of device fingerprints when time-frequency information is captured at the optimal scale.

Statistical Robustness and Confidence Analysis: The confidence intervals reported across all configurations underscore the statistical robustness of the proposed approach. Out of 72 total configurations (24 hyperparameter combinations \times 3 models), 46 configurations achieved confidence interval widths below 2.0%, of which 15 configurations achieved below 1.0% confidence intervals. These exceptionally tight confidence intervals demonstrate that the frequency-domain representations yield deterministic device fingerprints with minimal stochastic variation. The configurations achieving zero-width confidence intervals were concentrated in longer- L_{seg} , higher- $p_{overlap}$, and higher- R settings, where the models had access to sufficiently rich spectral information to make perfect, unambiguous classifications. Few (8 configurations) exhibited wider confidence intervals of 3-4% corresponding to scenarios with reduced data availability or lower spectral

TABLE V
EVALUATION OF DL ACROSS ALL EXPERIMENTAL CONFIGURATIONS

L_{seg}	$p_{overlap}$	R	Model	STFT				CWT				
				Train (%)	Val (%)	Test (%)	F1	CI width	Train (%)	Val (%)	Test (%)	
100	0%	DeiT-Base	99.89	99.29	98.57	0.9857	1.25	100	99.55	97.23	0.972	1.88
		16 ViT-Small	98.82	97.41	92.41	0.914	2.95	99.98	99.73	97.86	0.9784	1.61
		EfficientViT	99.25	98.57	97.68	0.9768	1.7	99.93	99.64	96.61	0.9649	2.14
	50%	DeiT-Base	99.91	98.75	98.12	0.981	1.61	99.73	94.64	95.18	0.9472	2.42
		32 ViT-Small	99.88	98.84	98.39	0.9838	1.39	99.84	99.64	98.48	0.9847	1.43
		EfficientViT	99.96	98.75	97.41	0.9733	1.79	99.96	99.73	98.66	0.9865	1.34
	100	DeiT-Base	100	96.61	93.93	0.9384	2.77	99.91	99.46	99.46	0.9946	0.8
		64 ViT-Small	99.95	96.79	93.21	0.9285	2.86	100	99.73	99.29	0.9928	0.8
		EfficientViT	99.98	96.79	92.59	0.9237	3.12	99.91	99.82	99.02	0.99	1.16
500	0%	DeiT-Base	99.93	98.84	98.84	0.9884	1.21	99.98	99.73	97.41	0.9736	1.79
		16 ViT-Small	99.91	98.84	98.21	0.982	1.61	99.98	99.64	97.5	0.9746	1.7
		EfficientViT	99.98	99.11	98.39	0.9839	1.34	99.98	99.91	96.52	0.9636	2.05
	50%	DeiT-Base	99.93	98.57	95.98	0.956	2.28	99.98	99.82	99.55	0.9955	0.8
		32 ViT-Small	99.88	98.66	97.32	0.9723	1.92	99.91	99.73	99.73	0.9973	0.54
		EfficientViT	99.96	98.57	97.68	0.9762	1.7	99.96	99.91	99.91	0.9991	0.27
	100	DeiT-Base	99.98	96.25	94.64	0.946	2.59	100	99.73	99.73	0.9973	0.62
		64 ViT-Small	99.95	96.96	95.18	0.9511	2.5	99.98	99.55	99.29	0.9928	1.07
		EfficientViT	99.93	97.05	95.27	0.9513	2.46	99.95	99.91	99.46	0.9946	0.89
200	0%	DeiT-Base	100	100	99.52	0.9952	1.19	100	98.81	97.14	0.9714	3.1
		16 ViT-Small	100	100	99.52	0.9952	1.19	99	98.57	97.62	0.9762	2.98
		EfficientViT	99.95	99.76	99.29	0.9928	1.67	99.95	99.29	94.05	0.9365	4.52
	50%	DeiT-Base	100	100	95.71	0.9971	3.81	100	99.76	100	1	0
		32 ViT-Small	99.9	99.52	95.48	0.9548	3.81	99.95	99.29	95	0.943	4.05
		EfficientViT	100	100	97.62	0.9758	3.1	100	100	99.29	0.9928	1.67
	100	DeiT-Base	100	100	99.05	0.9905	1.79	100	100	99.29	0.9929	1.67
		64 ViT-Small	99.9	99.76	97.38	0.9734	3.1	100	100	99.29	0.9929	1.67
		EfficientViT	100	99.76	98.1	0.9809	2.62	99.81	100	100	1	0
500	0%	DeiT-Base	100	99.52	99.76	0.9976	0.71	100	98.81	98.57	0.9857	2.14
		16 ViT-Small	99.95	99.29	99.76	0.9976	0.71	99.86	98.57	98.81	0.988	1.9
		EfficientViT	100	100	99.76	0.9976	0.71	99.86	99.05	97.86	0.9785	2.62
	50%	DeiT-Base	99.95	99.52	96.52	0.9952	1.19	100	99.76	99.52	0.9952	1.19
		32 ViT-Small	99.95	99.52	99.05	0.9904	1.79	99.95	99.52	99.05	0.9905	1.67
		EfficientViT	99.95	99.52	99.52	0.9952	1.19	100	100	1	0	
	100	DeiT-Base	100	99.52	98.81	0.9877	2.14	100	100	98.57	0.9856	2.27
		64 ViT-Small	99.95	99.52	98.33	0.9832	2.62	100	100	100	1	0
		EfficientViT	99.95	99.76	98.81	0.9881	2.14	100	100	100	1	0

Notation: The green highlights the best performance within the $p_{overlap}$ in the L_{seg} .

resolution, where test-set samples exhibit slightly higher classification ambiguity. These wider intervals still represent strong performance with accuracy over 95%.

D. Cross-Configuration Evaluation

Evaluation of 24-configuration demonstrated excellent performance under matched training and test conditions. To further assess model robustness, the best-performing model from each configuration was evaluated on held-out out-of-distribution (OOD) evaluation sets of three segment lengths ($L_{seg} \in \{100, 200, 500\}$) and four overlap fractions ($p_{overlap} \in \{0\%, 25\%, 50\%, 75\%\}$) which were not used for training, validation or test. This OOD set simulates realistic deployment scenarios where observation windows may vary in duration and $p_{overlap}$, enabling assessment of model generalization beyond matched training conditions. The results of cross-configuration are summarized in Table VI.

For STFT-trained models, those trained on shorter segments and lower R generalize far better across all test conditions. Models trained with $L_{seg} = 100$ (at $R = 16, 32$) consistently

achieve 98–99% accuracy across all L_{seg} and $p_{overlap}$. It maintains or even improves performance when tested on longer unseen segments, achieving over 99% accuracy on $L_{seg} = 200, 500$, exceedingly even the 98.81% baseline from matched training conditions. This suggests that short-segment training compels models to focus on core, transferable device-specific features that generalize across temporal scales. In contrast, models trained on longer segments ($L_{seg} = 500$) perform poorly (29–48% accuracy) when tested on shorter windows, likely due to overfitting to long-term temporal patterns. Across all configurations, $p_{overlap}$ variation caused minimal degradation (less than 1–2% deviation), confirming that STFT-based models learn overlap-invariant, stable representations.

CWT models demonstrate strong consistency across $p_{overlap}$ conditions but high sensitivity to L_{seg} . When trained on $L_{seg} = 100$ with $R = 32, 64$, they achieve near-perfect accuracy (99.76–99.94%) on matching L_{seg} test sets with OOD $p_{overlap}$ but collapse to 22–33% accuracy on longer segments. Conversely, models trained on $L_{seg} = 500$ (e.g., $R = 32, p =$

TABLE VI
EVALUATION OF BEST MODELS ACROSS ODD SET FOR CROSS-CONFIGURATION EVALUATION

Method	L_{seg}	R	Best Model	Accuracy on ODD Evaluation Set (%)											
				$L_{seg} = 100$				$L_{seg} = 200$				$L_{seg} = 500$			
				$p=0\%$	$p=25\%$	$p=50\%$	$p=75\%$	$p=0\%$	$p=25\%$	$p=50\%$	$p=75\%$	$p=0\%$	$p=25\%$	$p=50\%$	$p=75\%$
STFT	16	DeiT-Base ($p=50\%$)	98.57	98.33	98.81	98.33	100	100	99.76	99.76	97.38	96.9	99.52	100	
		EfficientViT ($p=50\%$)	97.62	98.1	97.62	97.38	99.52	99.29	99.29	99.52	98.81	98.33	100	99.76	
		ViT-Small ($p=50\%$)	95.24	94.29	94.76	93.1	82.86	82.86	82.62	81.67	77.86	77.14	78.33	78.1	
	500	DeiT-Base ($p=50\%$)	29.52	30	29.52	30.48	79.29	79.76	81.43	83.57	99.52	99.76	99.76	100	
		ViT-Small ($p=50\%$)	62.86	63.57	63.33	65	85	85.71	86.67	90.24	99.29	99.52	99.52	99.52	
		EfficientViT ($p=50\%$)	47.86	47.38	47.62	48.57	83.81	83.57	84.29	83.81	99.05	98.57	98.81	98.57	
CWT	16	Vit-Small ($p=50\%$)	98.33	97.38	97.14	97.38	69.52	71.9	70	70.24	22.62	23.57	23.57	24.76	
		Vit-Small ($p=50\%$)	99.76	99.76	99.29	99.05	82.38	83.81	82.86	81.43	31.19	32.86	30.95	31.43	
		DeiT-Base ($p=50\%$)	99.76	100	100	100	92.62	91.9	90.95	92.14	30.48	32.38	31.9	32.86	
	500	DeiT-Base ($p=0\%$)	30	28.33	30.24	29.05	56.19	56.67	53.33	56.19	97.86	97.14	98.57	97.86	
		DeiT-Base ($p=50\%$)	51.9	51.9	54.05	50.71	64.76	64.29	64.05	66.43	100	100	100	100	
		DeiT-Base ($p=50\%$)	47.86	50.71	48.57	47.62	79.52	77.62	78.1	79.29	98.57	98.33	98.57	98.1	

Notation: p denotes the $p_{overlap}$. The red border indicates test set with configuration that the best model was trained on, the rest are ODD set.

0%) reach perfect accuracy across all $p_{overlap}$ settings for the same segment length yet drop to around 52% when tested on shorter segments. This pattern indicates that while CWT's multi-resolution nature enables precise modeling within a fixed temporal scale, it fails to generalize when the temporal context changes, as learned wavelet scales become misaligned with the new segment structure. Similar to STFT-trained models, $p_{overlap}$ variation caused minimal degradation (less than 1% standard deviation), confirming overlap-invariance in CWT.

Across all ViT models, those trained with $p_{overlap} = 50\%$ consistently demonstrated the best robustness and performance across cross-configuration evaluation sets, except for one CWT model ($L_{seg} = 500, R = 32, p = 0\%$). This advantage arises from smoother temporal transitions that help models learn segment-length-independent features. Notably, even though the same number of spectrograms (400) are used for training, the $p_{overlap} = 50\%$ setting requires only half the raw packet data compared to the non-overlapping case (refer to Table IV) yet still achieves superior accuracy and stability. Overall, STFT models trained on short segments ($L_{seg} = 100$) and lower spectral resolutions ($R = 16, 32$) show the strongest robustness, maintaining high accuracy across varying L_{seg} and $p_{overlap}$ conditions. Whereas CWT models achieve perfect accuracy only when training and deployment L_{seg} match, but their performance deteriorates sharply otherwise.

E. Discussion

STFT employs uniform frequency bins (fixed resolution Δf) across all time points, producing highly regular grid-like spectrograms with clear horizontal bands and vertical striations as observed in Fig. 3. This uniform structure enables robust cross-segment generalization because frequency bins remain valid regardless of L_{seg} , explaining why STFT-trained models on $L_{seg} = 100$ generalize well (99%+ accuracy) to unseen $L_{seg} = 200, 500$ ODD test windows. In contrast, CWT employs adaptive scale-dependent resolution where coarse scales capture low frequencies with poor temporal precision while fine scales capture high frequencies with excellent

temporal precision, producing hierarchical wavelet decompositions visible as nested patterns in Fig. 3. This adaptive resolution enables CWT to achieve perfect classification in many instances within matched L_{seg} by optimally allocating resolution across the observed frequency-time space. However, the scale-dependent patterns become fundamentally misaligned when L_{seg} change. The visual divergence between CWT $L_{seg} = 100$ and $L_{seg} = 500$ spectrograms (densely packed high-resolution patterns in 100-packet windows versus extended low-frequency details in 500-packet windows) reflects learned scales that are incompatible across segment-length shifts. This scale-dependence explains CWT's perfect in-distribution accuracy and severe cross-segment performance collapse. This is because learned wavelet scales perfectly encode device signatures within matched L_{seg} lengths but become fundamentally misaligned when tested on different durations. Therefore, for practical implementation, STFT offers robustness to variable deployment conditions and superior cross-segment generalization, while CWT provides theoretically optimal feature extraction within constrained operational contexts where segment lengths are fixed and data volume permits fine-resolution multi-scale analysis.

VI. CONCLUSION

This paper presents CONTEX-T, a novel framework demonstrating that encrypted IoT traffic remains vulnerable to contextual privacy exploitation through spectral analysis using ViT. By transforming raw packet-length sequences into rich time-frequency feature representations, the framework achieved exceptional device classification accuracy, with several configurations reaching perfect classification. The comprehensive factorial evaluation across multiple hyperparameter configurations revealed that packet-length distributions encode deterministic, device-specific signatures robust to strong encryption protocols. STFT-based models demonstrated superior cross-segment generalization, maintaining consistent high accuracy across variable observation windows, making them practical for real-world

deployment. Conversely, CWT models achieved optimal performance within matched training conditions but exhibited segment-length sensitivity. The exceptionally tight confidence intervals confirm statistical robustness and deterministic extraction. While these findings highlight the need for privacy-preserving defenses that obfuscate metadata and traffic patterns, the development of such defenses represents a limitation of this research and lies outside its scope. Therefore, this work establishes an important foundation for future research into countermeasures against passive, undetectable reconnaissance attacks in IoT networks.

REFERENCES

- [1] Y. Cui, F. Liu, X. Jing, and J. Mu, "Integrating Sensing and Communications for Ubiquitous IoT: Applications, Trends, and Challenges," *IEEE Netw.*, vol. 35, no. 5, pp. 158–167, Sept. 2021.
- [2] H. N. Thakur, A. Al Hayajneh, K. Thakur, A. Kamruzzaman, and M. L. Ali, "A Comprehensive Review of Wireless Security Protocols and Encryption Applications," in *2023 IEEE World AI IoT Congress (AIoIoT)*, Seattle, WA, USA: IEEE, June 2023, pp. 0373–0379.
- [3] T. Yadav and A. M. Rao, "Technical Aspects of Cyber Kill Chain," in *International Symposium on Security in Computing and Communication*, Kochi, India: Springer, Aug. 2015, pp. 438–452.
- [4] M. L. Ali, S. Ismat, K. Thakur, A. Kamruzzaman, Z. Lue, and H. N. Thakur, "Network Packet Sniffing and Defense," in *2023 IEEE 13th Annual Computing and Communication Workshop and Conference (CCWC)*, Las Vegas, NV, USA: IEEE, Mar. 2023, pp. 0499–0503.
- [5] C. Sheng *et al.*, "Network Traffic Fingerprinting for IIoT Device Identification: A Survey," *IEEE Trans. Ind. Inform.*, vol. 21, no. 5, pp. 3541–3554, May 2025.
- [6] S. Dong, L. Shu, Q. Xia, J. Kamruzzaman, Y. Xia, and T. Peng, "Device Identification Method for Internet of Things Based on Spatial-Temporal Feature Residuals," *IEEE Trans. Serv. Comput.*, vol. 17, no. 6, pp. 3400–3416, Nov. 2024.
- [7] Y. Feng, Y. Zhang, H. He, W. Zhang, and D. Wang, "An IoT Device Identification Method Using Extracted Fingerprint From Sequence of Traffic Grayscale Images," *IEEE Trans. Dependable Secure Comput.*, vol. 21, no. 6, pp. 5737–5754, Nov. 2024.
- [8] Q. Lu, Z. Xu, H. Zhang, and H. Xian, "SLIoTDI: Scalable and Lightweight IoT Device Identification With Session-Level Grayscale Fingerprinting and Adversarial Training," *IEEE Trans. Netw. Serv. Manag.*, pp. 1–1, 2025.
- [9] Y. Xiao *et al.*, "IoT-SCNet: Semi-supervised Contrastive Network Traffic Images Learning for IoT Device Identification," *IEEE Internet Things J.*, pp. 1–1, 2025.
- [10] L. Tang, Y. Jia, Y. Qian, S. Yi, and P. Yuan, "Human Activity Recognition Based on Mixed CNN With Radar Multi-Spectrogram," *IEEE Sens. J.*, vol. 21, no. 22, pp. 25950–25962, Nov. 2021.
- [11] A. Satt, S. Rozenberg, and R. Hoory, "Efficient Emotion Recognition From Speech Using Deep Learning on Spectrograms," in *Interspeech*, 2017, pp. 1089–1093. Accessed: Nov. 14, 2025.
- [12] A. S. Khan, Z. Ahmad, J. Abdullah, and F. Ahmad, "A Spectrogram Image-Based Network Anomaly Detection System Using Deep Convolutional Neural Network," *IEEE Access*, vol. 9, pp. 87079–87093, 2021.
- [13] Z. Ahmad, A. S. Khan, K. Zen, and F. Ahmad, "MS-ADS : Multistage Spectrogram image-based Anomaly Detection System for IoT security," *Trans. Emerg. Telecommun. Technol.*, vol. 34, no. 8, p. e4810, Aug. 2023.
- [14] N. Dillbary, R. Yozhevitch, A. Dvir, R. Dubin, and C. Hajaj, "Hidden in Time, Revealed in Frequency: Spectral Features and Multiresolution Analysis for Encrypted Internet Traffic Classification," in *2024 IEEE 21st Consumer Communications & Networking Conference (CCNC)*, Las Vegas, NV, USA: IEEE, Jan. 2024, pp. 266–271.
- [15] J. Huang, B. Chen, B. Yao, and W. He, "ECG Arrhythmia Classification Using STFT-based Spectrogram and Convolutional Neural Network," *IEEE Access*, vol. 7, pp. 92871–92880, 2019.
- [16] Z. Zeng, R. Kaur, S. Siddagangappa, T. Balch, and M. Veloso, "From Pixels to Predictions: Spectrogram and Vision Transformer for Better Time Series Forecasting," in *4th ACM International Conference on AI in Finance*, Brooklyn NY USA: ACM, Nov. 2023, pp. 82–90.
- [17] A. Sivanathan *et al.*, "Classifying IoT Devices in Smart Environments Using Network Traffic Characteristics," *IEEE Trans. Mob. Comput.*, vol. 18, no. 8, pp. 1745–1759, Aug. 2019.
- [18] C. Duan, H. Gao, G. Song, J. Yang, and Z. Wang, "BytelIoT: A Practical IoT Device Identification System Based on Packet Length Distribution," *IEEE Transaction on Network Service Management*, vol. 19, no. 2, pp. 1717–1728, June 2022.
- [19] K. Kostas, M. Just, and M. A. Lones, "IoTDevID: A Behavior-Based Device Identification Method for the IoT," *IEEE Internet Things J.*, vol. 9, no. 23, pp. 23741–23749, Dec. 2022.
- [20] J. Zhao, Q. Li, J. Sun, M. Dong, K. Ota, and M. Shen, "Efficient IoT Device Identification via Network Behavior Analysis Based on Time Series Dictionary," *IEEE Internet Things J.*, vol. 11, no. 3, pp. 5129–5142, Feb. 2024.
- [21] J. Zhao, Q. Li, Y. Hong, and M. Shen, "MetaRockETC: Adaptive Encrypted Traffic Classification in Complex Network Environments via Time Series Analysis and Meta-Learning," *IEEE Trans. Netw. Serv. Manag.*, vol. 21, no. 2, pp. 2460–2476, Apr. 2024.
- [22] L. Cohen, "Time-frequency Analysis," *Englewood Cliffs*, 1995.
- [23] S. Mallat, *A Wavelet Tour of Signal Processing*. Academic press, 1999.
- [24] C. S. Lessard, *Signal Processing of Random Physiological Signals*. Morgan & Claypool Publishers, 2006.
- [25] C. Torrence and G. P. Compo, "A Practical Guide to Wavelet Analysis," *Bull. Am. Meteorol. Soc.*, vol. 79, no. 1, pp. 61–78, 1998.
- [26] M. Priyadarshini, M. Bajaj, L. Prokop, and M. Berhanu, "Perception of Power Quality Disturbances Using Fourier, Short-Time Fourier, Continuous and Discrete Wavelet Transforms," *Sci. Rep.*, vol. 14, no. 1, p. 3443, 2024.
- [27] I. Daubechies, "The Wavelet Transform, Time-frequency Localization and Signal Analysis," *IEEE Transaction on Information Theory*, vol. 36, no. 5, pp. 961–1005, 2002.
- [28] S. G. Mallat, "A Theory for Multiresolution Signal Decomposition: the Wavelet Representation," *IEEE Trans. Pattern Anal. Mach. Intell.*, vol. 11, no. 7, pp. 674–693, 2002.
- [29] B. Jawerth and W. Sweldens, "An Overview of Wavelet Based Multiresolution Analyses," *SIAM Rev.*, vol. 36, no. 3, pp. 377–412, 1994.
- [30] H. Touvron, M. Cord, M. Douze, F. Massa, A. Sablayrolles, and H. Jégou, "Training data-efficient image transformers & distillation through attention," in *International Conference on Machine Learning*, PMLR, 2021, pp. 10347–10357.
- [31] A. Dosovitskiy, "An Image is Worth 16x16 Words: Transformers for Image Recognition at Scale," *ArXiv Prepr. ArXiv201011929*, 2020.
- [32] X. Liu, H. Peng, N. Zheng, Y. Yang, H. Hu, and Y. Yuan, "Efficientvit: Memory Efficient Vision Transformer with Cascaded Group Attention," in *IEEE/CVF conference on computer vision and pattern recognition*, 2023, pp. 14420–14430.
- [33] K. Han *et al.*, "A Survey on Vision Transformer," *IEEE Trans. Pattern Anal. Mach. Intell.*, vol. 45, no. 1, pp. 87–110, 2022.
- [34] S. Khan, M. Naseer, M. Hayat, S. W. Zamir, F. S. Khan, and M. Shah, "Transformers in Vision: A Survey," *ACM Comput. Surv. CSUR*, vol. 54, no. 10s, pp. 1–41, 2022.